ACS OMEGA

http://pubs.acs.org/journal/acsodf

Article

# Low-Temperature $NH_3$-SCR over Hierarchical $MnO_x$ Supported on Montmorillonite Prepared by Different Methods

Xianlong Zhang, Shi Jin, Shiwen Liu, Yazhong Chen, Cheng Fang, Kui Wang, Xinyu Wang, Xueping Wu,* and Junwei Wang

Cite This: *ACS Omega* 2023, 8, 13384−13395

Read Online

ACCESS | Metrics & More | Article Recommendations

**ABSTRACT:** Hierarchical $MnO_x$ pillared or supported on montmorillonite were prepared by three methods, i.e., impregnation (IM), chemical precipitation (CP), and in situ deposition (SP). The catalysts were characterized by low-temperature $N_2$ adsorption (BET), XRD, XPS, SEM, TEM, $H_2$-TPR, $NH_3$-TPD, NO-TPD, TPSR, in situ DRIFTS, and evaluation of catalytic performance for $NH_3$-SCR. The best catalytic performance was obtained for catalysts prepared by SP in terms of activity and selectivity, obtaining >90% NO conversion with >95% selectivity to $N_2$ in 100−300 °C and GHSV of 70,000 $h^{-1}$. Compared to IM and CP, SP greatly simplified catalyst preparation, resulting in higher BET surface areas; a spongy pore structure; more highly dispersed, pillared $MnO_x$ species; and higher density of acid sites distributed on catalysts surface, which all contributed to its superior performance for $NH_3$-SCR. The activity for low-temperature $NH_3$-SCR of manganese catalysts could be widely tailored by preparation methods.

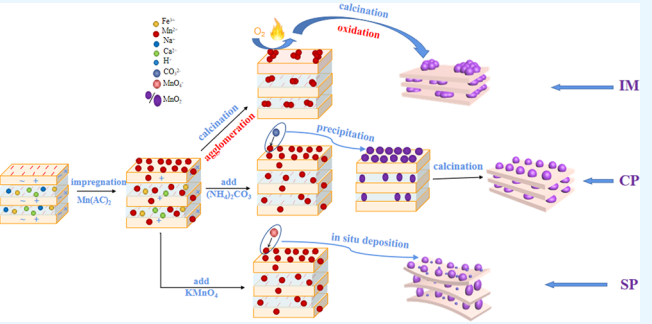


## 1. INTRODUCTION

Nitrogen oxides ($NO_x$) from both mobile (e.g., automobile engine combustion emission) and stationary (e.g., coal-fired power plants) sources are persistent air pollution contributors, leading to a series of environmental problems such as photochemical smog, tropospheric ozone, and acid rain.[1,2] Selective catalytic reduction of $NO_x$ with $NH_3$ ($NH_3$-SCR) is an efficient process for $NO_x$ abatement.[3] Although $V_2O_5/TiO_2$ catalysts have been successfully commercialized, the high operation temperature, poor $N_2$ selectivity, and toxicity of vanadium hinder their wide application.[4,5] Thus, efficient $NH_3$-SCR catalysts without vanadium species have attracted much attention. $MnO_x$-based catalysts show high de$NO_x$ performance at 100−300 °C, and their performance could be tailored through the strong interaction between support and $MnO_x$.[6−9]

Using natural clay like montmorillonites (MMTs) as support efficiently decreases the cost of catalysts. Pillared clays such as MMT are efficient catalysts at around 300 °C, showing good resistance to $SO_2$ and high $N_2$ selectivity.[10,11] The factors influencing the de$NO_x$ performance include parent clays, pillaring agents, and intercalation. By using different metal oxides as pillaring agents, catalytic performance could be widely and finely tailored.[12−16]

Recent progress in $NH_3$-SCR shows that the suitable temperature window is 100−250 °C. The de$NO_x$ performance of PICLs in this temperature range deserves an in-depth study. However, current PICL preparation methods are complex and time-consuming. Recently, we developed an in situ deposition method for preparing $MnO_x$-based catalysts through the fast redox reaction between $Mn^{2+}$ and $MnO_4^-$ in an aqueous solution, which show high-performance, low-temperature $NH_3$-SCR.[17,18] Thus, in this work, based upon clay, pillaring agent, and introduction method screening, we found that pillaring and modification could be combined into one process to obtain hierarchical $MnO_x$, e.g., pillared and supported $MnO_x$, simultaneously. The catalyst gave the best catalytic performance in comparison with those prepared by IM or CP. Under working conditions of $T$ = 100−300 °C, GHSV = 70,000 $h^{-1}$, and 1000 ppm NO concentration, almost complete NO conversion and >95% $N_2$ selectivity were obtained. The SP method greatly simplified the preparation and simultaneously overcame the limitation of cation exchange capacity (CEC) of MMT. A series of characterizations were performed to clarify the reason for the best performance of the catalyst prepared by SP.

**Received:** February 10, 2023
**Accepted:** March 21, 2023
**Published:** March 30, 2023

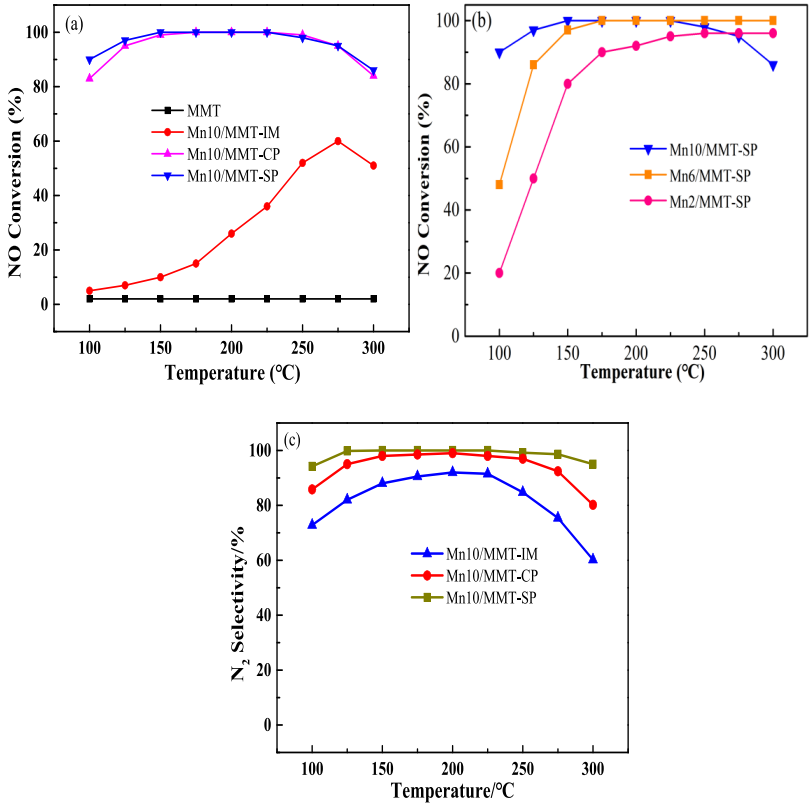


**Figure 1.** (a) NO conversion over MMT, Mn10/MMT-IM, Mn10/MMT-CP, or Mn10/MMT-SP. (b) NO conversion over Mn2/MMT-SP, Mn6/MMT-SP, and Mn10/MMT-SP. (c) $N_2$ selectivity. Working conditions: $[NH_3]$ = [NO] = 1000 ppm, $[O_2]$ = 3%, $[H_2O]$ = 5%, $N_2$ as the balance gas, GHSV = 70,000 $h^{-1}$, and total flow rate = 350 mL·$min^{-1}$.

## 2. EXPERIMENTAL SECTION

**2.1. Materials.** MMT with a CEC of 86 mmol/100 g was purchased from Borun Casting Material Co. Ltd., Henan, China. The elemental composition of MMT was determined by X-ray fluorescence (XRF). The received clays were dried, milled, and sieved to obtain a granular size less than 0.127 mm for use. Analytical-grade $Mn(AC)_2{\cdot}4H_2O$, $KMnO_4$, and $(NH_4)_2CO_3$ were purchased from Sinopharm Chemical Reagent Co. Ltd., China, and used as received.

**2.2. Catalyst Preparation Methods.** *2.2.1. Impregnation.* The catalyst was prepared by the incipient wetness impregnation method. MMT (20.0 g) was placed into a $Mn(Ac)_2$ solution (8.909 g $Mn(AC)_2{\cdot}4H_2O$ in a certain amount of deionized water; the volume is equal to the suction capacity of 20.0 g dry MMT) and aged for 24 h. Then, the sample was dried at 110 °C overnight and calcined at 300 °C for 3 h. The powder was pelletized, crushed, and sieved to 20−40 mesh granular size and labeled as Mn10/MMT-IM.

*2.2.2. Chemical Precipitation.* $Mn(Ac)_2{\cdot}4H_2O$ (8.909 g) was dissolved in deionized water, and then 20.0 g of MMT was added into the solution. The mixture was aged under moderate stirring for 24 h. $(NH_4)_2CO_3$ (5.714 g) was dissolved in deionized water to give a concentration of 2.0 M. Then, the solution was dropwisely added into the impregnated MMT and stirred for 24 h to accomplish precipitation. Then, the mixture was aged for 12 h, washed several times, and filtered. The filtration cake was dried at 110 °C overnight and then calcined at 300 °C for 3 h. Thus obtained powder was pelletized, crushed, and sieved to collect 20−40 mesh granules described as Mn10/MMT-CP.

*2.2.3. In Situ Deposition.* $KMnO_4$ (2.30 g) was added into 10.0 mL of deionized water to form a solution with a concentration of 0.15 M. $Mn(Ac)_2{\cdot}4H_2O$ (5.346 g) was dissolved in deionized water (equal to the suction capacity of 20.0 g dry MMT). MMT (20.0 g) was added into the $Mn(Ac)_2$ solution, and then the mixture was aged for 24 h. Then, the as-prepared $KMnO_4$ solution was added to complete the redox reaction described in eq 1. Then, the mixture was aged, washed several times, and filtered. The filtration cake was dried at 110 °C overnight. Thus obtained powder was pelletized, crushed, and sieved to obtain 20−40 mesh granules denoted as Mn10/MMT-SP. Likewise, Mn2/MMT-SP and Mn6/MMT-SP were also prepared.

$$2KMnO_4 + 3Mn^{2+} + 2H_2O \rightarrow 5MnO_2 + 4H^+ + 2K^+ \quad (1)$$

**2.3. Catalyst Characterization.** The instrumental information and operational details on SEM, TEM, XRD, low-temperature $N_2$ adsorption (BET), $NH_3$-TPD, and XPS can be found in our previous work.[19] XRF (XRF-1800, Shimadzu, Japan) was carried out to determine the elemental compositions. NO-TPD was performed on a self-made microreactor-mass spectrometer (Hiden-QIC20) system. The experimental procedures for NO-TPSR are described below. First, 0.5 g (0.3 mL) of the catalyst was charged into a quartz reactor; after $NH_3$ adsorption until saturation, the residual $NH_3$ in the pipeline was purged with Ar flux. Then, flux (1000 ppm NO, 3% $O_2$, 5% $H_2O$, and balanced $N_2$, total flow 350 mL·$min^{-1}$, GHSV 70,000 $h^{-1}$) was introduced to perform surface reaction under temperature programmed working conditions. A portable flue gas analyzer (Testo 350 XL) was


https://doi.org/10.1021/acsomega.3c00718
ACS Omega 2023, 8, 13384−13395

used to record the NO concentration of the flux at the outlet. The experimental procedures for $NH_3$-TPSR were performed in similar ways by changing NO into $NH_3$.

The in situ DRIFTS was performed on an FTIR spectrometer (Nicolet iS50). The scanning range was 400−4000 $cm^{-1}$. The catalyst was initially pretreated in a 30 mL·$min^{-1}$ argon flow at 50 °C for 30 min followed by $NH_3$/NO adsorption at 50 °C in the argon atmosphere until saturation and ending with Ar purging for 30 min. After the pretreatment stage, the $NH_3$/NO-TPD experiment was started. Under the argon flow, the temperature was programmed to increase from 50 to 300 °C, and the reflected infrared spectra were recorded continuously. The background spectrum from the pretreatment stage was automatically subtracted from the sample spectrum.

**2.4. Catalytic Reaction.** The denitrification performance was evaluated in a quartz fixed-bed reactor of 15 mm inner diameter under atmospheric pressure. A simulated flue gas containing 1000 ppm NO, 1000 ppm $NH_3$, 3% $O_2$, 5% $H_2O$, and balancing $N_2$ was used and tested from 100 to 300 °C. The simulated flue gas had a flow rate of 350 mL·$min^{-1}$, which corresponds to a GHSV of 70,000 $h^{-1}$. The concentrations of $NO_x$ at the inlet and outlet of the reactor were measured online by an MRU OPTIMA7 flue gas analyzer with an accuracy of ±3%. The concentration of $N_2O$ at the outlet of the reactor was determined with a TD-400-$N_2O$ analyzer with an accuracy of ±2%. The concentration of $NH_3$ was detected by a GT-1000-$NH_3$ analyzer an with accuracy of ±1%. The conversion of NO and selectivity to $N_2$ were calculated according to eqs 2 and 3, respectively.

$$\text{NO conversion (\%)} = 100\% \times \frac{[\text{NO}]_{\text{in}} - [\text{NO}]_{\text{out}}}{[\text{NO}]_{\text{in}}} \quad (2)$$

$$N_2 \text{ selectivity (\%)} = \left(1 - \frac{2[N_2O]}{[\text{NO}]_{\text{in}} - [\text{NO}]_{\text{out}} + [NH_3]_{\text{in}} - [NH_3]_{\text{out}}}\right) \times 100\% \quad (3)$$

where $[\text{NO}]_{\text{in}}$ and $[\text{NO}]_{\text{out}}$ are the concentrations of $NH_3$ in ppm at the inlet or outlet of the reactor, $[NH_3]_{\text{in}}$ and $[NH_3]_{\text{out}}$ are the concentrations of NO in ppm at the inlet or outlet of the reactor, and $[N_2O]$ is the concentration of $N_2O$ in ppm at the outlet of the reactor, respectively.

## 3. RESULTS AND DISCUSSION

**3.1. The Denitrification Performance.** The denitrification performance in terms of NO conversion for MMT catalysts prepared by three different methods with 10.0 wt % manganese loading is shown in Figure 1a; for catalysts prepared by SP with different manganese loadings, the results are shown in Figure 1b. MMT shows no catalytic activity for SCR in 100−300 °C, suggesting that the loading of manganese plays a vital role. Mn10/MMT-SP shows the best performance followed by Mn10/MMT-CP and then Mn10/MMT-IM. Surprisingly, Mn10/MMT-SP achieves >90% NO conversion even at 100 °C (GHSV = 70,000 $h^{-1}$), which is very attractive for low-temperature SCR applications.[17,20] Figure 1b shows the influences of manganese loading on NO conversion. With the increase of manganese loading from 2 to 10 wt %, NO conversion is obviously enhanced at temperatures below 150 °C. Interestingly, Mn2/MMT-SP shows better performance than Mn10/MMT-IM, which strongly indicates that the dispersion of manganese species on MMT is the dominating factor of denitrification performance rather than manganese loading.[21,22] Therefore, it seems that precipitation (CP) or deposition (SP) can efficiently increase the dispersion of $MnO_x$ on the surface or in layers of MMT. Particularly, SP provides fast redox reaction and fast nucleation in the aqueous solution, thus generating fine $MnO_x$, which is also evidenced by TEM.

From Figure 1c, we find that Mn10/MMT-SP shows not only high NO conversion but also high selectivity to $N_2$. Generally, with the increase of reaction temperature, the selectivity to $N_2$ decreases slowly because of the ammonia oxidation. For Mn10/MMT-SP, almost no $N_2O$ was detected, and the selectivity to $N_2$ is close to 100% (>98.5%) at 100−150 °C. However, for Mn10/MMT-CP, the selectivity to $N_2$ is within 94.0−95.5% at 100−150 °C. Mn10/MMT-IM shows the poorest selectivity to $N_2$, obtaining selectivity to $N_2$ only in the range of 91.0−92.0%. The trend between $N_2$ selectivity and reaction temperature is similar for three catalysts, as shown in Figure1c.

**3.2. Characterization Results and Analysis.** *3.2.1. XRD.* Figure 2 shows the XRD patterns of MMT and catalysts with

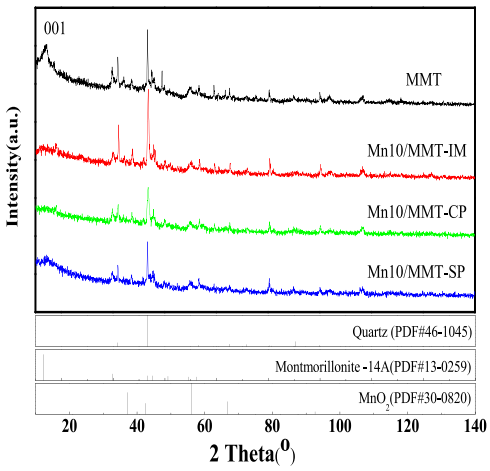


**Figure 2.** XRD patterns of MMT, Mn10/MMT-IM, Mn10/MMT-CP, and Mn10/MMT-SP.

10 wt % manganese loading prepared by IM, CP, or SP, respectively. For MMT, major diffraction peaks are located at 2-theta values of 7.0, 19.85, 26.67, 27.59, 30.59, 34.60, and 36.04° (PDF#13-0259). The peak at 7.0° is attributed to the layer distance of the (001) lattice planes corresponding to a basal spacing of 1.26 nm. After subtracting the thickness of the silica layer (0.96 nm), the interlayer space is 0.30 nm. Moreover, the diffraction intensities corresponding to the (001) lattice plane of MMT in the three catalysts obviously decrease, which suggest the successful loading of $MnO_x$ into the interlayer spacing.[23,24] However, no diffraction peak corresponding to $MnO_x$ is observed, which suggests that $MnO_x$ exists in an amorphous state or low degree of crystallinity; pillared $MnO_x$ could not be detected by XRD.[25,26] Amorphous or pillared $MnO_x$ could provide rich oxygen vacancies that favor $NH_3$-SCR.[27]

*3.2.2. XRF.* The XRF results are listed in Table 1. The catalysts prepared by CP or SP show much lower $Na_2O$ contents (about 0.30 vs 1.17%), which strongly suggest that


https://doi.org/10.1021/acsomega.3c00718
ACS Omega 2023, 8, 13384−13395

Table 1. Composition of MMT and Catalysts Prepared by Different Methods Determined by XRF

| | content (wt %) | | | | | | | |
|---|---|---|---|---|---|---|---|---|
| samples | $SiO_2$ | $Al_2O_3$ | $K_2O$ | $Fe_2O_3$ | $Na_2O$ | MgO | $MnO_2$ | Mn |
| MMT | 70.98 | 15.10 | 5.37 | 3.34 | 1.74 | 1.25 | 0.00 | 0.00 |
| Mn2/MMT-SP | 69.73 | 14.73 | 5.96 | 3.48 | 0.32 | 1.14 | 2.77 | 1.75 |
| Mn6/MMT-SP | 65.57 | 13.66 | 6.34 | 3.33 | 0.33 | 1.02 | 7.86 | 4.97 |
| Mn10/MMT-SP | 61.23 | 12.93 | 6.42 | 3.05 | 0.34 | 0.95 | 13.17 | 8.32 |
| Mn10/MMT-CP | 63.53 | 13.29 | 4.87 | 3.05 | 0.38 | 1.03 | 11.78 | 7.45 |
| Mn10/MMT-IM | 61.33 | 13.21 | 4.66 | 3.11 | 1.17 | 1.07 | 13.54 | 8.56 |

$Na^+$ trapped between the interlayer of MMT could be exchanged with $Mn^{2+}$[28] and the ion-exchanged $Na^+$ could be removed through washing.

Comparing the $Na_2O$ contents in Mn2/MMT-SP, Mn6/MMT-SP, Mn10/MMT-SP, and Mn10/MMT-CP, we found that $Na_2O$ contents show little change with the increase of manganese loading. It could be ascribed to the fact that the ion exchange between $Na^+$ and $Mn^{2+}$ could reach equilibrium at a certain $Na^+$ concentration, and not all the $Na^+$ could be exchanged because of the high ionic strength of solution.[29] Table 1 also shows that $K_2O$ contents increase with manganese loading. The reason could be closely related with reaction 1. $K^+$ also could be partially exchanged into the layer spacing.

The consumption of $Mn^{2+}$ is sandwiched between the layers of MMT in in situ generated protons through the fast redox reaction 1. Simultaneously, some $K^+$ also could be ion-exchanged into the layer, which are difficult to remove through washing. As a result, the $K_2O$ contents in the catalysts prepared by SP are much higher than those by CP or IM. Interestingly, the inclusion of $K^+$ into the catalysts derived from SP does not deteriorate $NH_3$-SCR activity. This fact indicates that those $K^+$ located in the layers of MMT are quite different from the $K_2O$ deposited on the surface of catalyst, which is unfavorable for $NH_3$-SCR. It is worth noting that with the same manganese loading of 10.0 wt %, preparation methods influence the denitrification performance in terms of NO conversion and $N_2$ selectivity significantly. Therefore, the reason should be further probed.

*3.2.3. SEM.* The SEM images of samples are shown in Figure 3. The preparation methods show different degrees of modification for MMT. The layered structure of MMT, as shown in Figure 3a, can form interlayer channels with cations sandwiched inside. When $MnO_x$ were introduced by IM, as shown in Figure 3b, the removal of interlayer water results in the shrinkage of the MMT interlayer spacing. Most of the $MnO_x$ stay on the external edge of layers as aggregated particles, blocking the channels into the layer spacing, which are also confirmed by the pore volume and specific surface area results in Table 2. For Mn10/MMT-CP, as shown in Figure 3c, the laminar stack of MMT could be clearly observed, whereas $MnO_x$ were more uniformly dispersed on MMT layers, although partial agglomeration is observed. Additionally, the external edge of the MMT layer is partly filled with fine $MnO_x$, implying that precipitation could occur in the interlayer spacing of MMT. Mn10/MMT-SP, as shown in Figure 3d, presents the most distinctive structural morphology with flocculent $MnO_x$ loosely and uniformly dispersed on MMT. It is hard to distinguish the classic laminar stack of MMT due to the high coverage by $MnO_x$. The uniform distribution of porous and flocculent $MnO_x$ provides large specific surface areas and short internal mass transfer paths for the $NH_3$-SCR reaction, which could explain its high denitrification performance in the 100−300 °C range.[20]

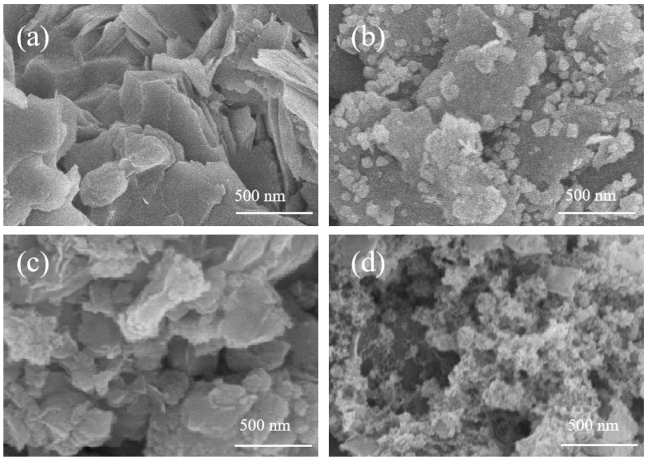


Figure 3. SEM of (a) MMT, (b) Mn10/MMT-IM, (c) Mn10/MMT-CP, and (d) Mn10/MMT-SP.

Table 2. Textural Properties of MMT and Catalysts Prepared by Different Methods

| samples | $S_{BET}$ ($m^2 \cdot g^{-1}$) | Average pore size (nm) | pore volume ($cm^3 \cdot g^{-1}$) |
|---|---|---|---|
| MMT | 37.5 | 50.1 | 0.091 |
| Mn10/MMT-IM | 26.6 | 85.2 | 0.099 |
| Mn10/MMT-CP | 70.2 | 10.3 | 0.170 |
| Mn10/MMT-SP | 100.2 | 19.1 | 0.210 |

*3.2.4. TEM.* The TEM images and Mn-EDS of samples are displayed in Figure 4. For MMT, the lamellar structure can be clearly observed in Figure 4a. An interlayer spacing of 1.101 nm is identified, as shown in Figure 4a-1. The agglomeration of $MnO_x$ in Mn10/MMT-IM is also confirmed by Figure 4b,b-2. Mn10/MMT-SP shows the highest dispersion of $MnO_x$, as shown in Figure 4d. HRTEM images shown in Figure 4b-1,c-1,d-1 correspond to the (100) plane of MnO (PDF#34-0394), the (101) plane of ramsdelite ($MnO_2$) (PDF#44-0142), and the (102) plane of akhtenskite ($MnO_2$) (PDF#30-0820), respectively. Different preparation methods result in the various kinds of $MnO_x$ with different valence state of manganese.

*3.2.5. Low-Temperature $N_2$ Adsorption.* Table 2 shows the specific surface area, pore volume, and average pore size of samples. The low specific surface area of Mn10/MMT-IM could be ascribed to the maldistribution of $MnO_x$ and the probable blocking of the access to the interlayer spacings after



https://doi.org/10.1021/acsomega.3c00718
ACS Omega 2023, 8, 13384−13395

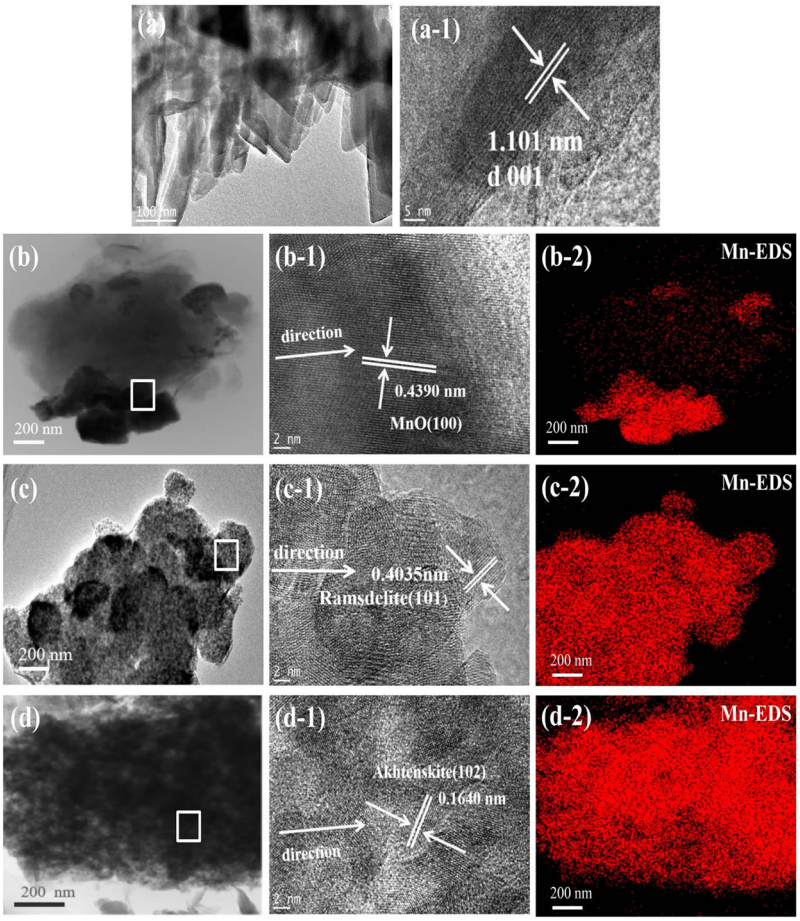


**Figure 4.** TEM images and Mn-EDS of (a) MMT, (b) Mn10/MMT-IM, (c) Mn10/MMT-CP, and (d) Mn10/MMT-SP.

calcination.[30] Mn10/MMT-SP shows much higher specific surface areas than MMT as a result of its highly spongy and porous structure. Compared to Mn10/MMT-CP, the supported $MnO_x$ on the surface of the MMT and $MnO_x$ pillared into the interlayers both contribute to the increased surface area and pore volume for Mn10/MMT-SP.

Figure 5 presents the $N_2$ adsorption and desorption curves and pore size distribution of the three catalysts. According to the IUPAC classification, the $N_2$ adsorption−desorption isotherms show a hysteresis loop of H3 type,[31] corresponding to the flat pores from the layered structures of MMT.[32] Under low pressures, $N_2$ shows a monolayer adsorption behavior. Consequently, the adsorption capacity is closely related with the micropore volume. Mn10/MMT-CP and Mn10/MMT-SP show much higher adsorption capacities at low pressures, which suggest that CP and SP methods can significantly increase the micropore volume (<2 nm). From Figure 5, we observe that the fraction of mesopore (2−50 nm) in Mn10/MMT-IM decreases but moderately increases in Mn10/MMT-CP, whereas it significantly increases in Mn10/MMT-SP. The higher specific surface area and the larger fraction of mesopore benefit the low-temperature $NH_3$-SCR,[33] as could be seen in Figure 1.

*3.2.6. XPS.* The XPS characterization was carried out to elaborate the valences of the elements on the sample surfaces. The Mn 2*p* and O 1*s* spectra are shown in Figure 6. The contents of manganese with different valence states are summarized in Table 3. As shown in Figure 6a, the binding energies of 642.0 and 653.8 eV are assigned to Mn $2p_{3/2}$ and

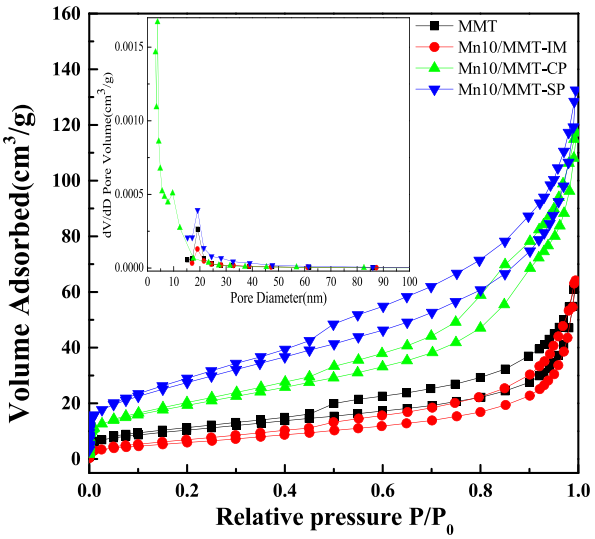


**Figure 5.** $N_2$ adsorption−desorption isotherms of MMT and catalysts prepared by different methods.

Mn $2p_{1/2}$ peaks, respectively.[6] After peak fitting, the Mn $2p_{3/2}$ peak could be divided into three individual peaks corresponding to $Mn^{2+}$ (641.0−641.8 eV), $Mn^{3+}$ (642.2−643.0 eV), and $Mn^{4+}$ (643.2−644.5 eV), respectively.[34,35] From Table 3, we find that Mn10/MMT-IM, Mn10/MMT-CP, and Mn10/MMT-SP catalysts show comparable amounts of $Mn^{3+}$ but quite different contents of $Mn^{4+}$. Mn10/MMT-SP shows the


https://doi.org/10.1021/acsomega.3c00718
ACS Omega 2023, 8, 13384−13395

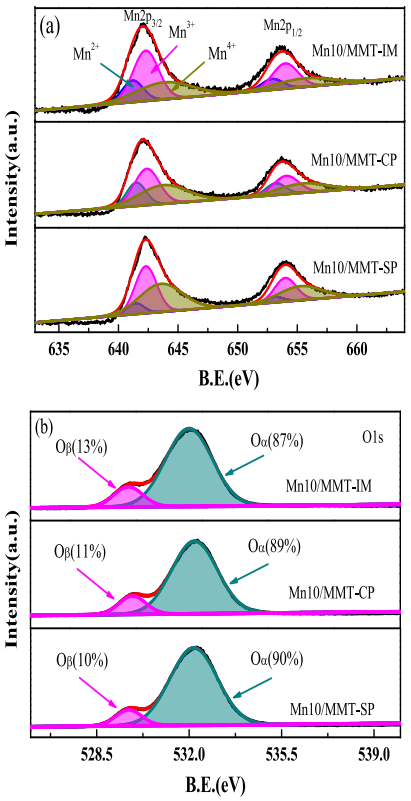


**Figure 6.** (a) XPS spectra of Mn2p3/2 of catalysts prepared by different methods. (b) XPS spectra of O 1*s* of catalysts prepared by different methods.

**Table 3. Surface Composition of Manganese with Different Valences in the Catalysts after Reaction**

| | binding energy (eV) | | | percentages (%) | | |
|---|---|---|---|---|---|---|
| samples | $Mn^{2+}$ | $Mn^{3+}$ | $Mn^{4+}$ | $Mn^{2+}$ | $Mn^{3+}$ | $Mn^{4+}$ |
| Mn10/MMT-IM | 641.19 | 642.29 | 643.85 | 16.79 | 47.86 | 35.36 |
| Mn10/MMT-CP | 641.49 | 642.37 | 643.76 | 19.89 | 40.39 | 39.72 |
| Mn10/MMT-SP | 641.42 | 642.30 | 643.57 | 7.61 | 42.33 | 50.06 |

highest concentration of $Mn^{4+}$ followed by Mn10/MMT-CP and then Mn10/MMT-IM. A previous work showed that $Mn^{4+}$ on the catalyst surface plays an irreplaceable role in $NH_3$-SCR. The higher content of $Mn^{4+}$ facilitates the oxygen vacancy formation and the redox cycle between $Mn^{4+}$ and $Mn^{3+}$, which is very important in $NH_3$-SCR.[17,36,37]

Oxygen vacancy formation and surface mobility of chemisorbed oxygen species can also affect low-temperature $NH_3$-SCR.[38,39] Two main signals of oxygen species were found after peak fitting, as shown in Figure 6b. The peak at about 530.0 eV is the surface lattice oxygen $O^{2-}$(denoted as $O_\beta$), and the peak at around 532.0 eV is surface chemisorbed oxygen $O^{2-}$ and $O^-$ in oxygen vacancies or defect sites (denoted as $O_\alpha$).[33] $O_\alpha$ is more active than $O_\beta$.[40] The redox process in $NH_3$-SCR involves lattice oxygen release and gas oxygen insertion into oxygen vacancy.[38] The abundant $O_\alpha$ adsorbed on the catalyst surface with good mobility is superior to lattice oxygen because the former can better oxidize NO into $NO_2$ and accelerate the SCR reaction.[41−43] For the three prepared catalysts, there are moderate differences in content, with 87, 89, and 90.0% surface $O_\alpha$ for Mn10/MMT-IM, Mn10/MMT-CP, and Mn10/MMT-SP, respectively. It seems that the surface $O_\alpha$ content of each catalyst is slightly coincident with the SCR performance of the catalyst, implying that the $O_\alpha$ coupled with various forms of $MnO_x$ may be related to the catalytic reaction.

*3.2.7. $H_2$-TPR.* It has been widely accepted that an efficient $NH_3$-SCR reaction demands a catalyst with good acid-redox features. The redox performance of MMT and catalysts was evaluated by $H_2$-TPR, and the results are shown in Figure 7

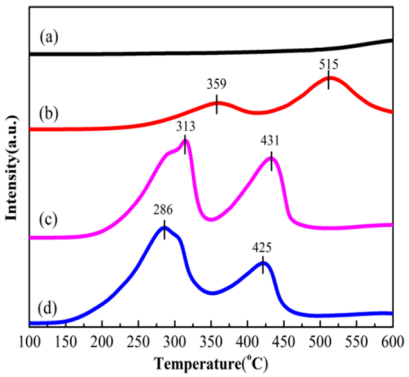


**Figure 7.** $H_2$-TPR profiles of (a) MMT, (b) Mn10/MMT-IM, (c) Mn10/MMT-CP, and (d) Mn10/MMT-SP.

**Table 4. The Peak Temperatures and Integrated Areas Calculated from $H_2$-TPR Curves**

| samples | peak temperatures (°C) | area (a.u.) | total areas (a.u.) |
|---|---|---|---|
| MMT | | | $0.2 \times 10^6$ |
| Mn10/MMT-IM | 359 | $0.42 \times 10^6$ | $1.27 \times 10^6$ |
| | 515 | $0.85 \times 10^6$ | |
| Mn10/MMT-CP | 313 | $1.07 \times 10^6$ | $2.06 \times 10^6$ |
| | 431 | $0.99 \times 10^6$ | |
| Mn10/MMT-SP | 286 | $1.31 \times 10^6$ | $2.13 \times 10^6$ |
| | 425 | $0.82 \times 10^6$ | |

and Table 4. For MMT, no peak is observed. For the three catalysts, two major peaks are observed, which could be attributed to the reduction of $MnO_2$ into $Mn_2O_3$ and then $Mn_2O_3$ into MnO, respectively.[34,43,44] However, TPR profiles of Mn10/MMT-CP and Mn10/MMT-SP are similar but quite different with that of Mn10/MMT-IM. The peak temperatures of Mn10/MMT-CP and Mn10/MMT-SP are much lower than that of Mn10/MMT-IM, indicating that the dispersion of $MnO_x$ and $Mn^{4+}$ contents follows the order Mn10/MMT-SP > Mn10/MMT-CP > Mn10/MMT-IM.[45]

Although similar $H_2$-TPR profiles were obtained for Mn10/MMT-CP and Mn10/MMT-SP, there are also some distinct details reflecting the differences in microstructure. First, either the starting temperature or the peak temperature for Mn10/MMT-SP is obviously lower than that of Mn10/MMT-CP, suggesting that the surface $MnO_x$ on Mn10/MMT-SP has better redox property. Second, the relative intensity of the two peaks in $H_2$-TPR of each catalysts varied obviously, reflecting the different contents of $Mn^{4+}$ and $Mn^{3+}$, which are also evidenced by the XPS results in Table 3. The peak areas of samples are shown Table 4, following the order Mn10/MMT-


https://doi.org/10.1021/acsomega.3c00718
ACS Omega 2023, 8, 13384−13395

SP > Mn10/MMT-CP > Mn10/MMT-IM. The large reduction peak areas reflect the high content of surface $Mn^{4+}$, whereas the lower reduction peak temperature could be attributed to the dispersion of $MnO_x$. Smaller particles are more readily reduced. Mn10/MMT-SP has the highest content of surface $Mn^{4+}$ and best dispersion of $MnO_x$, which result in the efficient conversion of NO into $NO_2$ at low temperature and promotes SCR performance.[46,47]

*3.2.8. $NH_3$-TPD.* $NH_3$-TPD experiments were performed to determine the quantity and strength of surface acids, which are important in $NH_3$-SCR.[48] As shown in Figure 8, the desorption

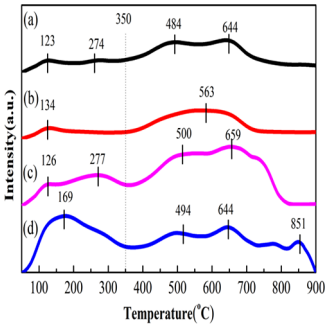


**Figure 8.** $NH_3$-TPD profiles of (a) MMT, (b) Mn10/MMT-IM, (c) Mn10/MMT-CP, and (d) Mn10/MMT-SP.

peaks below 200 °C are attributed to the surface Brønsted acid sites, whereas those above 200 °C with a wide temperature range result from $NH_3$ coordinated with the Lewis acid sites.[49] Desorption peak areas in the $NH_3$-TPD profiles could indirectly reflect the total number of acid sites.[17]

MMT shows desorption peaks at 123, 274, 484, and 644 °C, respectively. However, the peak areas below 250 °C are much smaller than those above 250 °C, which suggest that MMT mainly contains Lewis acid sites. Among the three catalysts, Mn10/MMT-SP shows a large peak centered at 169 °C, which is not present in both Mn10/MMT-IM and Mn10/MMT-CP. The reason is that SP intrinsically introduces protons into the interlayers of MMT when $Mn^{2+}$ is consumed by $MnO_4^-$, as described in eq 1. Those protons could not be washed away because of the strong charge interactions inside MMT spacings and consequently result in the high content of Brønsted acid sites in Mn10/MMT-SP. These Brønsted acid sites were crucial for the high performance of SCR at temperatures below 250 °C.[20]

*3.2.9. NO-TPD.* The adsorption of NO is also an important factor for $NH_3$-SCR.[50] Figure 9 shows the NO-TPD curves of MMT and catalysts, and the peak areas are listed in Table 5. $MnO_x$ loading significantly enhances NO adsorption with the order of Mn10/MMT-SP > Mn10/MMT-CP > Mn10/MMT-IM.

In the NO-TPD curve, the peaks below 200 °C are attributed to the decomposition of weak-binding nitrite species,[51] whereas the peaks above 260 °C are ascribed to the decomposition of bidentate or bridged nitrates.[52] Above 300 °C, desorption products include $N_2$, $O_2$, or $N_2O$ originated from decomposition. As $NH_3$-SCR is investigated below 300 °C in this work, we therefore limit the temperature range to 50−300 °C in the NO-TPD diagram. The integrated peak areas at temperatures below or above 200 °C can be used as an indicator for the relative amount of different species. From Table 5, we could see that the amounts of monodentate nitrite

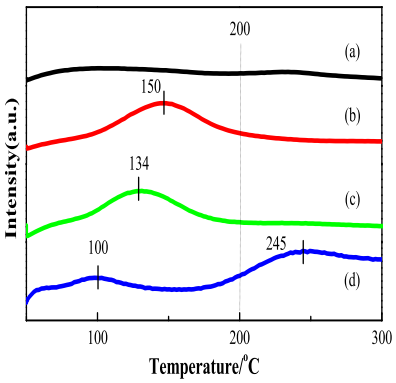


**Figure 9.** NO-TPD profiles of (a) MMT, (b) Mn10/MMT-IM, (c) Mn10/MMT-CP, and (d) Mn10/MMT-SP.

are similar. However, in the temperature range of 200−300 °C, Mn10/MMT-SP shows the maximum amount of moderate-binding nitrate species on the surface followed by Mn10/MMT-CP and then Mn10/MMT-IM. Stable nitrate species with high desorption temperature could cover some active sites, thereby deteriorating overall SCR performance.[53] Although Mn10/MMT-SP has a large amount of nitrate species, the main desorption peak temperature is within the range of 150−300 °C, suggesting that Mn10/MMT-SP possesses a large amount of active sites for NO adsorption with moderate adsorption strength. Mn10/MMT-IM shows active sites for NO adsorption in the range of 100−150 °C. The weak adsorption is insufficiently active for the following transformation in SCR; thus, lower catalytic performance is observed. Meanwhile, for Mn10/MMT-CP, the NO desorption peak was not observed in 200−300 °C, which suggests the low adsorption strength of NO, and the $NH_3$-SCR could proceed through the Eley−Rideal mechanism.

*3.2.10. TPSR.* TPSR was used to investigate the reaction between NO and the preadsorbed $NH_3$ under an oxidative environment, and the results are shown in Figure 10. At 100−400 °C, two inverted peaks are detected, which suggest the reaction between NO and the preadsorbed $NH_3$, thus decreasing the outlet NO concentration. The peak areas represent the total NO amount reacted with the preadsorbed $NH_3$. Thus, we integrated the inverted peaks of the samples in the temperature range of 100−300 °C. The NO treatment capacities of the samples are shown in Table 6. Mn10/MMT-SP and Mn10/MMT-CP show much higher performance than MMT and Mn10/MMT-IM, which is consistent with catalytic performance and the BET and $NH_3$-TPD results. Mn10/MMT-CP gives a similar NO conversion to Mn10/MMT-SP in the temperature range of 100−300 °C, as shown in Figure 1, which agrees well with the TPSR results. The selectivity to $N_2$ is about 5% lower than that of Mn10/MMT-SP, as shown in Figure 2. Thus, Mn10/MMT-SP shows the best performance, efficiently and selectively transforming $NO_x$ into $N_2$.

**3.3. In Situ DRIFTS.** *3.3.1. $NH_3$ Adsorption−Desorption.* In situ DRIFTS of $NH_3$ adsorption−desorption was performed to distinguish the Lewis and Brønsted acid sites, and the results are shown in Figure 11. After $NH_3$ absorption, MMT and catalysts both show an independent peak at 3250−3500 $cm^{-1}$, which could be ascribed to the O−H stretching vibration of surface hydroxyl and N−H stretching vibration of absorbed $NH_3$ on Lewis acid sites.[54,55] In this infrared band, there is an obvious competitive adsorption between $NH_3$ and $H_2O$. The


https://doi.org/10.1021/acsomega.3c00718
ACS Omega 2023, 8, 13384−13395

Table 5. The Integrated Peak Areas Calculated from $NH_3$-TPD or NO-TPD Curves

| samples | $NH_3$-TPD (V·s) | | NO-TPD (V·s) | | | |
|---|---|---|---|---|---|---|
| | $S_{(50-350\ °C)}$ | $S_{(350-900\ °C)}$ | $S_{total}$ | $S_{(50-200\ °C)}$ | $S_{(200-300\ °C)}$ | $S_{total}$ |
| MMT | $0.49 \times 10^{-7}$ | $1.33 \times 10^{-7}$ | $1.82 \times 10^{-7}$ | $0.14 \times 10^{-7}$ | $0.73 \times 10^{-8}$ | $0.21 \times 10^{-7}$ |
| Mn10/MMT-IM | $0.43 \times 10^{-7}$ | $1.18 \times 10^{-7}$ | $1.61 \times 10^{-7}$ | $0.26 \times 10^{-7}$ | $1.90 \times 10^{-8}$ | $0.45 \times 10^{-7}$ |
| Mn10/MMT-CP | $0.77 \times 10^{-7}$ | $1.98 \times 10^{-7}$ | $2.75 \times 10^{-7}$ | $0.34 \times 10^{-7}$ | $2.18 \times 10^{-8}$ | $0.56 \times 10^{-7}$ |
| Mn10/MMT-SP | $1.15 \times 10^{-7}$ | $1.81 \times 10^{-7}$ | $2.96 \times 10^{-7}$ | $0.33 \times 10^{-7}$ | $4.27 \times 10^{-8}$ | $0.76 \times 10^{-7}$ |

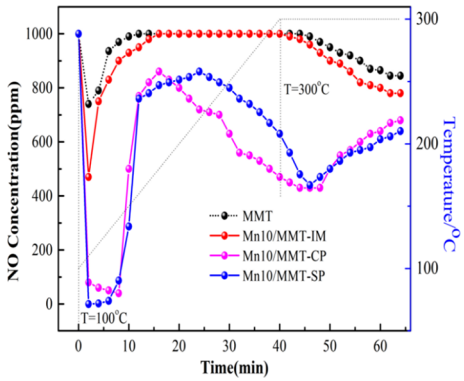


Figure 10. TPSR profile of MMT and catalysts prepared by different methods. Working conditions: $[NH_3]$ = [NO] = 1000 ppm, $[O_2]$ = 3%, $[H_2O]$ = 5%, $N_2$ as the balance gas, GHSV = 70,000 $h^{-1}$, and total flow rate = 350 mL·$min^{-1}$.

Table 6. NO Processing Capacities of Different Catalysts in Certain Temperature Ranges

| samples | average ability (mol·$g^{-1}$) | | |
|---|---|---|---|
| | 100−200 °C | 200−300 °C | 100−300 °C |
| MMT | $0.42 \times 10^{-4}$ | 0 | $0.21 \times 10^{-4}$ |
| Mn10/MMT-IM | $0.84 \times 10^{-4}$ | 0 | $0.43 \times 10^{-4}$ |
| Mn10/MMT-CP | $3.66 \times 10^{-4}$ | $2.67 \times 10^{-4}$ | $3.16 \times 10^{-4}$ |
| Mn10/MMT-SP | $3.98 \times 10^{-4}$ | $1.60 \times 10^{-4}$ | $2.79 \times 10^{-4}$ |

stable peaks that can still exist stably with the increase of temperature are attributed to $NH_3$ adsorbed by Lewis acid site, whereas the peaks that disappeared at high temperature are caused by the cleavage of the O−H bond. For the Mn10/MMT-SP catalyst, the adsorption capacity of $H_2O$ is obviously weaker than that of $NH_3$. The infrared bands of 3250 and 3445 $cm^{-1}$ should be attributed to the N−H stretching vibration of absorbed $NH_3$ on Lewis acid sites. In contrast, the Mn10/MMT-SP catalyst showed stronger and more stable Lewis acid sites. The influences of the preparation method on catalysts are also reflected in the infrared region of 1000−2000 $cm^{-1}$. For MMT, there is no infrared band in this region. After $MnO_x$ loading, each catalyst shows new infrared bands within 1000−2000 $cm^{-1}$. For Mn10/MMT-IM, as shown in Figure 11b, the band at 1650 $cm^{-1}$ belongs to $NH_4^+$ at a weak Brønsted acid site,[56] which disappears rapidly with the increase of temperature, indicating that the $NH_3$ connected to the weak Brønsted acid sites is unstable. In Figure 11c, for Mn10/MMT-CP, infrared bands of 1633 $cm^{-1}$ appear after $NH_3$ adsorption, which correspond to the stretching vibration of the N−H bond at the Brønsted acid sites. Compared with Mn10/MMT-IM, it can be seen that the peak intensity of Mn10/MMT-CP is higher at lower temperatures, and with the increase of temperature, the peak strength gradually decreases until it disappears at about 300 °C, indicating that Mn10/MMT-CP has higher acid strength and more Brønsted acid sites than Mn10/MMT-IM. Compared with Mn10/MMT-IM and Mn10/MMT-CP, Mn10/MMT-SP shows more acid sites, with three consecutive peaks in the range of 1250−1750 $cm^{-1}$. The bands of 1420 and 1665 $cm^{-1}$ are attributed to $NH_4^+$ formed at Brønsted acid sites, whereas the bands at 1550 $cm^{-1}$ are attributed to $NH_{3,ads}$ on Lewis acid sites.[57−59] As can be seen from Figure 11d, Mn10/MMT-SP remains its Lewis acid sites and Brønsted acid sites within 50−200 °C, which benefited low-temperature $NH_3$-SCR.

*3.3.2. NO Adsorption−Desorption.* To identify the types of nitrate or nitrite species on the catalyst surface, in situ DRTFTS of NO absorption is employed, and the results are shown in Figure 12. In the range of 3250−3500 $cm^{-1}$, the three catalysts all have peaks due to the stretching vibration of the O−H of surface hydroxyl.[55] However, because of the absence of competitive adsorption of $NH_3$ and $H_2O$, the absorption peaks of the three catalysts do not show significant difference. They all show a strong peak intensity at low temperatures that gradually disappears at about 150 °C. In the infrared band range of 1000−2000 $cm^{-1}$, characteristic peaks due to $NO_x$ adsorption appear. The characteristic bands at 1310, 1330, 1440, and 1540 $cm^{-1}$ are assigned to bidentate nitrate,[60] and the bands at 1273 and 1635 $cm^{-1}$ are attributed to bridged nitrate and monodentate nitrate, respectively.[54] From Figure 12, we could be seen that monodentate nitrate is unstable, whereas bridging nitrate or bidentate nitrate has better stability, which agrees well with the results by Li et al.[61] From Figure 12, Mn10/MMT-IM shows a monodentate nitrate, bridging nitrate, and bidentate nitrate, but the content of these species is very small. Mn10/MMT-CP and Mn10/MMT-SP show more bidentate nitrate species. It can be seen from Figure 12b,c that both catalysts have strong adsorption peaks in the range of 50−250 °C. When the temperature rises up to 250 °C, the peak decreases rapidly, indicating the fast desorption of NO at the temperature. The results agree with the catalytic performance, showing decreased denitrification activity when the temperature is higher than 250 °C. In addition, compared with Mn10/MMT-IM and Mn10/MMT-CP, the Mn10/MMT-SP catalyst has a larger adsorption peak area at about 200 °C, which also means that it has a wider temperature range for stable existence of nitrate, which could explain the fact that its catalytic activity is better.

## 4. CONCLUSIONS

Hierarchical $MnO_x$ supported on montmorillonite were prepared by three different methods. We combined impregnation and modification steps for PILC preparation into one step, which significantly simplified the preparation process. Among the three methods, impregnation resulted in aggregated $MnO_x$ with poor dispersion and denitrification performance due to the limitation of CEC of interlayer cations in montmorillonite with $Mn^{2+}$. The catalysts prepared by in situ deposition introduce not only more $MnO_x$ but also more protons into the interlayer spacings of montmorillonite, thus


https://doi.org/10.1021/acsomega.3c00718
ACS Omega 2023, 8, 13384−13395

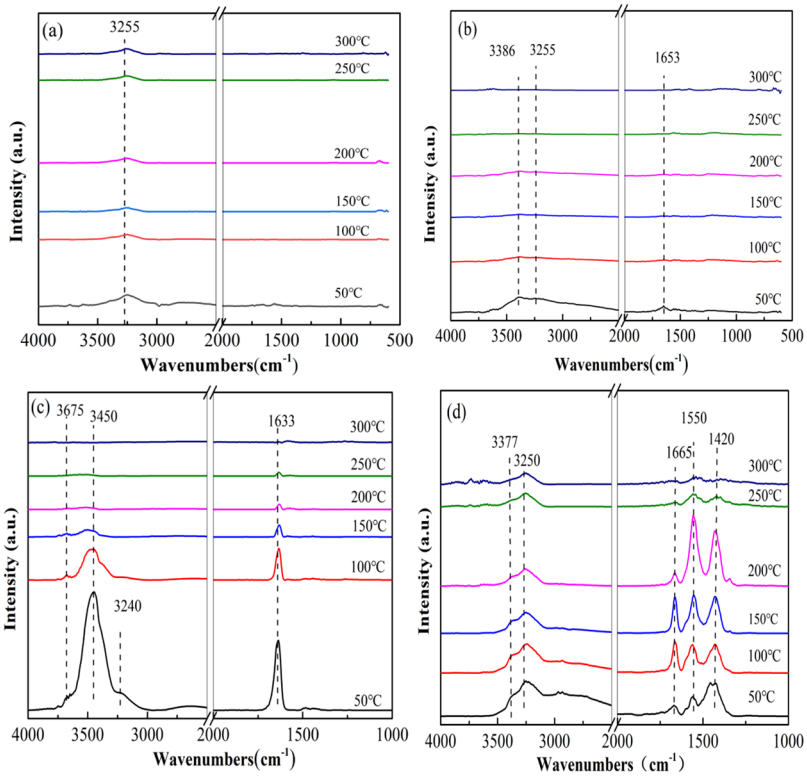


**Figure 11.** In situ DRIFTS spectra of $NH_3$ adsorption and desorption over the catalysts prepared by different methods: (a) MMT, (b) Mn10/MMT-IM, (c) Mn10/MMT-CP, and (d) Mn10/MMT-SP.

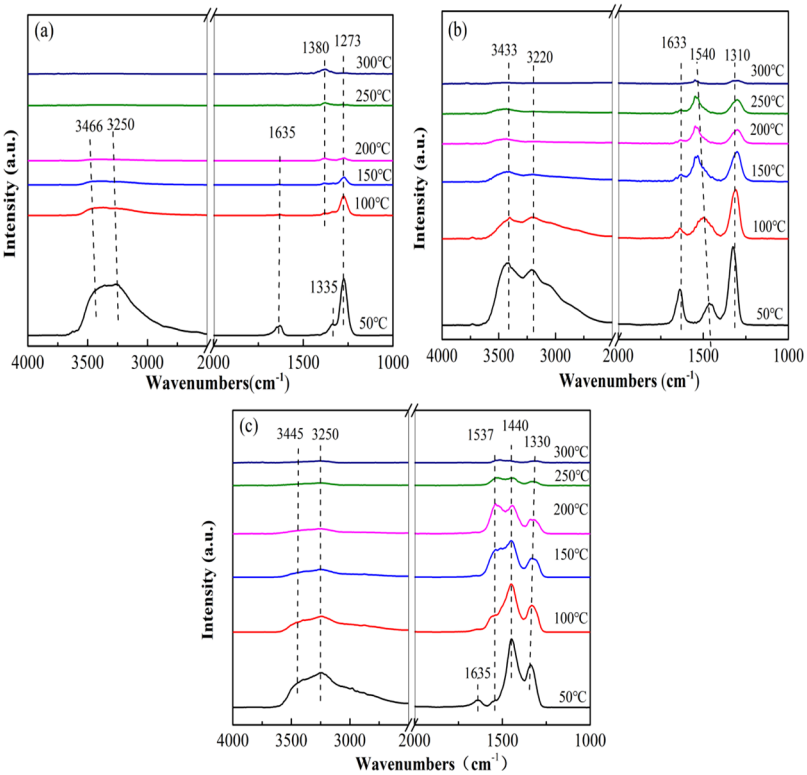


**Figure 12.** In situ DRIFTS spectra of NO absorption and related species on catalysts prepared by different methods: (a) Mn10/MMT-IM, (b) Mn10/MMT-CP, and (c) Mn10/MMT-SP.

increasing the Brønsted and Lewis acid sites simultaneously. Furthermore, the highly dispersed, fine amorphous $MnO_x$ species with a high content of $Mn^{4+}$ on the surface of montmorillonite endow Mn10/MMT-SP with enhanced adsorption of $NH_3$ and NO and better redox property, which result in the high denitrification performance, obtaining



https://doi.org/10.1021/acsomega.3c00718
ACS Omega 2023, 8, 13384−13395

complete conversion of NO in the low-temperature window of 100−250 °C under high GHSV working conditions with high selectivity to $N_2$.

## AUTHOR INFORMATION


### Corresponding Author

**Xueping Wu** − *School of Chemistry and Chemical Engineering and Anhui Province Key Laboratory of Advanced Catalytic Materials and Reaction Engineering, School of Chemistry and Chemical Engineering, Hefei University of Technology, Hefei 230009, China; Engineering Research Center of Advanced Composite Materials Design & Application of Anhui Province, Hefei 230009, China;* orcid.org/0000-0001-7265-9144; Email: xuepingw@ustc.edu.cn

### Authors

**Xianlong Zhang** − *School of Chemistry and Chemical Engineering and Anhui Province Key Laboratory of Advanced Catalytic Materials and Reaction Engineering, School of Chemistry and Chemical Engineering, Hefei University of Technology, Hefei 230009, China*

**Shi Jin** − *School of Chemistry and Chemical Engineering, Hefei University of Technology, Hefei 230009, China*

**Shiwen Liu** − *School of Chemistry and Chemical Engineering, Hefei University of Technology, Hefei 230009, China*

**Yazhong Chen** − *School of Chemistry and Chemical Engineering, Hefei University of Technology, Hefei 230009, China*

**Cheng Fang** − *School of Chemistry and Chemical Engineering, Hefei University of Technology, Hefei 230009, China*

**Kui Wang** − *School of Chemistry and Chemical Engineering, Hefei University of Technology, Hefei 230009, China*

**Xinyu Wang** − *School of Chemistry and Chemical Engineering, Hefei University of Technology, Hefei 230009, China*

**Junwei Wang** − *College of Chemistry and Chemical Engineering, Anqing Normal University, Anqing 246011, China*

Complete contact information is available at: https://pubs.acs.org/10.1021/acsomega.3c00718


### Notes

The authors declare no competing financial interest.

## ACKNOWLEDGMENTS

This study was financially supported in part by the National Natural Science Foundation of China (no. 51872070).

## REFERENCES


(1) Qian, L.; Zhao, B.; Wang, H.; Bao, G.; Hu, Y.; Xu, C. C.; Long, H. Valorization of the spent catalyst from flue gas denitrogenation by improving bio-oil production from hydrothermal liquefaction of pinewood sawdust. *Fuel* **2022**, *312*, No. 122804.

(2) Liu, W.; Gao, Z.; Sun, M.; Gao, J.; Wang, L.; Zhao, X.; Yang, R.; Yu, L. One-pot synthesis of $Cr_\alpha Mn_\beta CeTiO_x$ mixed oxides as $NH_3$-SCR catalysts with enhanced low-temperature catalytic activity and sulfur resistance. *Chem. Eng. Sci.* **2022**, *251*, No. 117450.

(3) Luo, J.; Kamasamudram, K.; Currier, N.; Yezerets, A. $NH_3$-TPD methodology for quantifying hydrothermal aging of Cu/SSZ-13 SCR catalysts. *Chem. Eng. Sci.* **2018**, *190*, 60−67.

(4) Bozbağ, S. E. Kinetic model comparison and elucidation of mass transfer limitations in $NH_3$-SCR reactors using Vanadia based washcoats with different thicknesses. *Chem. Eng. Sci.* **2021**, *246*, No. 116892.

(5) Li, J.; Zhang, C.; Li, Q.; Gao, T.; Yu, S.; Tan, P.; Fang, Q.; Chen, G. Promoting mechanism of $SO_2$ resistance performance by anatase $TiO_2$ {001} facets on Mn-Ce/$TiO_2$ catalysts during $NH_3$-SCR reaction. *Chem. Eng. Sci.* **2022**, *251*, No. 117438.

(6) Damma, D.; Pappas, D.; Boningari, T.; Smirniotis, P. Study of Ce, Sb, and Y exchanged titania nanotubes and superior catalytic performance for the selective catalytic reduction of $NO_x$. *Appl. Catal. B: Environ.* **2021**, *287*, No. 119939.

(7) Ettireddy, P. R.; Ettireddy, N.; Mamedov, S.; Boolchand, P.; Smirniotis, P. G. Surface characterization studies of $TiO_2$ supported manganese oxide catalysts for low temperature SCR of NO with $NH_3$. *Appl. Catal. B: Environ.* **2007**, *76*, 123−134.

(8) Wu, Z.; Jiang, B.; Liu, Y. Effect of transition metals addition on the catalyst of manganese/titania for low-temperature selective catalytic reduction of nitric oxide with ammonia. *Appl. Catal. B: Environ.* **2008**, *79*, 347−355.

(9) Xu, H.; Zhang, Q.; Qiu, C.; Lin, T.; Gong, M.; Chen, Y. Tungsten modified $MnO_x$−$CeO_2$/$ZrO_2$ monolith catalysts for selective catalytic reduction of $NO_x$ with ammonia. *Chem. Eng. Sci.* **2012**, *76*, 120−128.

(10) Gil, A.; Korili, S. A.; Vicente, M. A. Recent advances in the control and characterization of the porous structure of pillared clay catalysts. *Catal. Rev.* **2008**, *50*, 153−221.

(11) Yang, R. T.; Chen, J. P.; Kikkinides, E. S.; Cheng, L. S.; Cichanowicz, J. E. Pillared clays as superior catalysts for selective catalytic reduction of nitric oxide with ammonia. *Ind. Eng. Chem. Res.* **1992**, *31*, 1440−1445.

(12) Chmielarz, L.; Kuśtrowski, P.; Zbroja, M.; Gil-Knap, B.; Datka, J.; Dziembaj, R. SCR of NO by $NH_3$ on alumina or titania pillared montmorillonite modified with Cu or Co: Part II. Temperature programmed studies. *Appl. Catal. B: Environ.* **2004**, *53*, 47−61.

(13) Han, Z.; Yu, Q.; Xue, Z.; Liu, K.; Qin, Q. Sm-doped manganese-based Zr−Fe polymeric pillared interlayered montmorillonite for low temperature selective catalytic reduction of $NO_x$ by $NH_3$ in metallurgical sintering flue gas. *RSC Adv.* **2018**, *8*, 42017−42024.

(14) Cheng, J.; Ye, Q.; Zheng, C.; Cheng, S.; Kang, T.; Dai, H. Effect of ceria loading on Zr-pillared clay catalysts for selective catalytic reduction of NO with $NH_3$. *New J. Chem.* **2019**, *43*, 10850−10858.

(15) Xu, D.; Wu, W.; Wang, P.; Deng, J.; Yan, T.; Zhang, D. Boosting the alkali/heavy metal poisoning resistance for NO removal by using iron-titanium pillared montmorillonite catalysts. *J. Hazard. Mater.* **2020**, *399*, No. 122947.

(16) Zha, K.; Kang, L.; Feng, C.; Han, L.; Li, H.; Yan, T.; Maitarad, P.; Shi, L.; Zhang, D. Improved $NO_x$ reduction in the presence of alkali metals by using hollandite Mn−Ti oxide promoted Cu-SAPO-34 catalysts. *Environ. Sci-Nano.* **2018**, *5*, 1408−1419.

(17) Zhang, X.; Wu, Q.; Diao, Q.; Wang, J.; Xiao, K.; Yang, B.; Wu, X. Performance study for $NH_3$-SCR at low temperature based on different methods of Mnx/SEP catalyst. *Chem. Eng. J.* **2019**, *370*, 364−371.

(18) Zhang, X.; Wang, P.; Wu, X.; Lv, S.; Dai, J. Application of $MnO_x$/HNTs catalysts in low-temperature NO reduction with $NH_3$. *Catal. Commun.* **2016**, *83*, 18−21.

(19) Zhang, X.; Zhang, X.; Yang, X.; Chen, Y.; Wu, X. CeMn/$TiO_2$ catalysts prepared by different methods for enhanced low-temperature $NH_3$-SCR catalytic performance. *Chem. Eng. Sci.* **2021**, *238*, No. 116588.

(20) Zhang, X.; Hu, X.; Liu, S.; Chen, Y.; Jin, S.; Wang, X.; Wang, J.; Xiao, K.; Wu, X. MnOx-pillared rectorite prepared by in situ deposition as efficient catalysts for low-temperature $NH_3$-SCR: The influences of manganese (II) precursors. *J. Environ. Chem. Eng.* **2022**, *10*, No. 107318.

(21) Guo, R.; Sun, X.; Liu, J.; Pan, W.; Li, M.; Liu, S.; Sun, P.; Liu, S. Enhancement of the $NH_3$-SCR catalytic activity of MnTiOx catalyst by the introduction of Sb. *Appl. Catal. A* **2018**, *558*, 1−8.

(22) Luo, S.; Zhou, W.; Xie, A.; Wu, F.; Yao, C.; Li, X.; Zuo, S.; Liu, T. Effect of $MnO_2$ polymorphs structure on the selective catalytic

reduction of $NO_x$ with $NH_3$ over $TiO_2$−Palygorskite. *Chem. Eng. J.* **2016**, *286*, 291−299.
(23) Barama, S.; Dupeyrat-Batiot, C.; Capron, M.; Bordes-Richard, E.; Bakhti-Mohammedi, O. Catalytic properties of Rh, Ni, Pd and Ce supported on Al-pillared montmorillonites in dry reforming of methane. *Catal. Today* **2009**, *141*, 385−392.
(24) Zang, S.; Zhang, G.; Qiu, W.; Song, L.; Zhang, R.; He, H. Resistance to $SO_2$ poisoning of $V_2O_5/TiO_2$-PILC catalyst for the selective catalytic reduction of NO by $NH_3$. *Chin. J. Catal.* **2016**, *37*, 888−897.
(25) Thirupathi, B.; Smirniotis, P. G. Effect of Nickel as Dopant in $Mn/TiO_2$ Catalysts for the Low-Temperature Selective Reduction of NO with $NH_3$. *Catal. Lett.* **2011**, *141*, 1399−1404.
(26) Damma, D.; Boningari, T.; Ettireddy, P. R.; Reddy, B. M.; Smirniotis, P. G. Direct Decomposition of $NO_x$ over $TiO_2$ Supported Transition Metal Oxides at Low Temperatures. *Ind. Eng. Chem. Res.* **2020**, *57*, 16615−16621.
(27) Fang, D.; Xie, J.; Hu, H.; Yang, H.; He, F.; Fu, Z. Identification of $MnO_x$ species and Mn valence states in $MnO_x/TiO_2$ catalysts for low temperature SCR. *Chem. Eng. J.* **2015**, *271*, 23−30.
(28) Kabadagi, A.; Chikkamath, S.; Kobayashi, S.; Manjanna, J. Organo-modified Fe-montmorillonite as a solid acid catalyst for reduction of nitroarenes and Biginelli reactions. *Appl. Clay Sci.* **2020**, *189*, No. 105518.
(29) Wang, Y.; Gong, Y.; Lin, N.; Jiang, H.; Wei, X.; Liu, N.; Zhang, X. Cellulose hydrogel coated nanometer zero-valent iron intercalated montmorillonite (CH-MMT-n$Fe^0$) for enhanced reductive removal of Cr(VI): Characterization, performance, and mechanisms. *J. Mol. Liq.* **2022**, *347*, No. 118355.
(30) Boxiong, S.; Hongqing, M.; Chuan, H.; Xiaopeng, Z. Low temperature $NH_3$−SCR over Zr and Ce pillared clay based catalysts. *Fuel Process. Technol.* **2014**, *119*, 121−129.
(31) Chen, Y.; Zhang, Y.; Feng, X.; Li, J.; Liu, W.; Ren, S.; Yang, J.; Liu, Q. In situ deposition of 0D $CeO_2$ quantum dots on $Fe_2O_3$-containing solid waste $NH_3$-SCR catalyst: Enhancing $redo_x$ and $NH_3$ adsorption ability. *Waste Manage.* **2022**, *149*, 323−332.
(32) Thommes, M.; Kaneko, K.; Neimark, A. V.; Olivier, J. P.; Rodriguez-Reinoso, F.; Rouquerol, J.; Sing, K. S. W. Physisorption of gases, with special reference to the evaluation of surface area and pore size distribution (IUPAC Technical Report). *Pure Appl. Chem.* **2015**, *87*, 1051−1069.
(33) Zuo, H.; Xu, D.; Liu, W.; Dan, H.; Liu, X.; Lin, S.; Hou, P. Heat-treated dolomite-palygorskite clay supported $MnO_x$ catalysts prepared by various methods for low temperature selective catalytic reduction (SCR) with $NH_3$. *Appl. Clay Sci.* **2018**, *152*, 276−283.
(34) Yang, N.; Guo, R.; Pan, W.; Chen, Q.; Wang, Q.; Lu, C. The promotion effect of Sb on the Na resistance of $Mn/TiO_2$ catalyst for selective catalytic reduction of NO with $NH_3$. *Fuel* **2016**, *169*, 87−92.
(35) Liu, J.; Li, X.; Li, R.; Zhao, Q.; Ke, J.; Xiao, H.; Wang, L.; Liu, S.; Tadé, M.; Wang, S. Facile synthesis of tube-shaped Mn-Ni-Ti solid solution and preferable Langmuir-Hinshelwood mechanism for selective catalytic reduction of $NO_x$ by $NH_3$. *Appl. Catal. A: Gen.* **2018**, *549*, 289−301.
(36) Pappas, D. K.; Boningari, T.; Boolchand, P.; Smirniotis, P. G. Novel manganese oxide confined interweaved titania nanotubes for the low-temperature Selective Catalytic Reduction (SCR) of $NO_x$ by $NH_3$. *J. Catal.* **2016**, *334*, 1−13 http://dx.doi.org/10.1016/j.jcat.2015.11.013.
(37) Zhang, Z.; Li, J.; Tian, J.; Zhong, Y.; Zou, Z.; Dong, R.; Gao, S.; Xu, W.; Tan, D. The effects of Mn-based catalysts on the selective catalytic reduction of $NO_x$ with $NH_3$ at low temperature: A review. *Fuel Process. Technol.* **2022**, *230*, No. 107213.
(38) Ren, S.; Yang, J.; Zhang, T.; Jiang, L.; Long, H.; Guo, F.; Kong, M. Role of cerium in improving NO reduction with $NH_3$ over Mn−Ce/ASC catalyst in low-temperature flue gas. *Chem. Eng. Res. Des.* **2018**, *133*, 1−10.
(39) Peng, Y.; Chang, H.; Dai, Y.; Li, J. Structural and Surface Effect of $MnO_2$ for Low Temperature Selective Catalytic Reduction of NO with $NH_3$. *Procedia Environmental Sciences.* **2013**, *18*, 384−390.
(40) Li, L.; Zhang, L.; Ma, K.; Zou, W.; Cao, Y.; Xiong, Y.; Tang, C.; Dong, L. Ultra-low loading of copper modified $TiO_2/CeO_2$ catalysts for low-temperature selective catalytic reduction of NO by $NH_3$. *Appl. Catal. B: Environ.* **2017**, *207*, 366−375.
(41) Xiong, Y.; Tang, C.; Yao, X.; Zhang, L.; Li, L.; Wang, X.; Deng, Y.; Gao, F.; Dong, L. Effect of metal ions doping (M=$Ti^{4+}$, $Sn^{4+}$) on the catalytic performance of $MnO_x/CeO_2$ catalyst for low temperature selective catalytic reduction of NO with $NH_3$. *Appl. Catal. A: Gen.* **2015**, *495*, 206−216.
(42) Fang, D.; He, F.; Xie, J. Characterization and performance of common alkali metals and alkaline earth metals loaded $Mn/TiO_2$ catalysts for $NO_x$ removal with $NH_3$. *J. Energy Inst.* **2019**, *92*, 319−331.
(43) Thirupathi, B.; Smirniotis, P. G. Nickel-doped $Mn/TiO_2$ as an efficient catalyst for the low-temperature SCR of NO with $NH_3$: Catalytic evaluation and characterizations. *J. Catal.* **2012**, *288*, 74−83.
(44) France, L. J.; Yang, Q.; Li, W.; Chen, Z.; Guang, J.; Guo, D.; Wang, L.; Li, X. Ceria modified $FeMnO_x$-Enhanced performance and sulphur resistance for low-temperature SCR of $NO_x$. *App. Catal. B: Environ.* **2017**, *206*, 203−215.
(45) Thirupathi, B.; Pappas, D. K.; Smirniotis, P. G. Metal oxide-confined interweaved titania nanotubes M/TNT (M = Mn, Cu, Ce, Fe, V, Cr, and Co) for the selective catalytic reduction of $NO_x$ in the presence of excess oxygen. *J. Catal.* **2018**, *365*, 320−333.
(46) Zhang, G.; Han, W.; Zhao, H.; Zong, L.; Tang, Z. Solvothermal synthesis of well-designed ceria-tin-titanium catalysts with enhanced catalytic performance for wide temperature $NH_3$-SCR reaction. *Appl. Catal. B: Environ.* **2018**, *226*, 117−126.
(47) Xie, J.; Fang, D.; He, F.; Chen, J.; Fu, Z.; Chen, X. Performance and mechanism about $MnO_x$ species included in $MnO_x/TiO_2$ catalysts for SCR at low temperature. *Catal. Commun.* **2012**, *28*, 77−81.
(48) Jia, Y.; Jiang, J.; Zheng, R.; Guo, L.; Yuan, J.; Zhang, S.; Gu, M. Insight into the reaction mechanism over PMoA for low temperature $NH_3$-SCR: A combined In-situ DRIFTs and DFT transition state calculations. *J. Hazard. Mater.* **2021**, *412*, No. 125258.
(49) Kwon, D. W.; Nam, K. B.; Hong, S. C. Influence of tungsten on the activity of a Mn/Ce/W/Ti catalyst for the selective catalytic reduction of NO with $NH_3$ at low temperatures. *Appl. Catal. A: Gen.* **2015**, *497*, 160−166.
(50) Fang, C.; Shi, L.; Li, H.; Huang, L.; Zhang, J.; Zhang, D. Creating hierarchically macro−/mesoporous $Sn/CeO_2$ for the selective catalytic reduction of NO with $NH_3$. *RSC Adv.* **2016**, *6*, 78727−78736.
(51) Ma, L.; Cheng, Y.; Cavataio, G.; McCabe, R. W.; Fu, L.; Li, J. In situ DRIFTS and temperature-programmed technology study on $NH_3$-SCR of $NO_x$ over Cu-SSZ-13 and Cu-SAPO-34 catalysts. *Appl. Catal. B: Environ.* **2014**, *156-157*, 428−437.
(52) Lian, Z.; Liu, F.; He, H.; Shi, X.; Mo, J.; Wu, Z. Manganese−niobium mixed oxide catalyst for the selective catalytic reduction of $NO_x$ with $NH_3$ at low temperatures. *Chem. Eng. J.* **2014**, *250*, 390−398.
(53) Peng, Y.; Li, J.; Si, W.; Li, X.; Shi, W.; Luo, J.; Fu, J.; Crittenden, J.; Hao, J. Ceria promotion on the potassium resistance of $MnO_x/TiO_2$ SCR catalysts: An experimental and DFT study. *Chem. Eng. J.* **2015**, *269*, 44−50.
(54) Tang, N.; Liu, Y.; Wang, H.; Wu, Z. Mechanism study of NO catalytic oxidation over $MnO_x/TiO_2$ catalysts. *J. Phys. Chem. C* **2011**, *115*, 8214−8220.
(55) Kröcher, O.; Elsener, M. Chemical deactivation of $V_2O_5/WO_3$−$TiO_2$ SCR catalysts by additives and impurities from fuels, lubrication oils, and urea solution: I. Catalytic studies. *Appl. Catal. B: Environ.* **2008**, *77*, 215−227.
(56) Zhu, Y.; Zhang, Y.; Xiao, R.; Huang, T.; Shen, K. Novel holmium-modified Fe-$Mn/TiO_2$ catalysts with a broad temperature window and high sulfur dioxide tolerance for low-temperature SCR. *Catal. Commun.* **2017**, *88*, 64−67.
(57) Wang, P.; Yan, L.; Gu, Y.; Kuboon, S.; Li, H.; Yan, T.; Shi, L.; Zhang, D. Poisoning-resistant $NO_x$ reduction in the presence of


https://doi.org/10.1021/acsomega.3c00718
*ACS Omega* 2023, 8, 13384−13395

alkaline and heavy metals over H-SAPO-34-supported Ce-promoted Cu-based catalysts. *Environ. Sci. Technol.* **2020**, *54*, 6396−6405.
(58) Ma, Z.; Wu, X.; Feng, Y.; Si, Z.; Weng, D. Effects of $WO_3$ doping on stability and $N_2O$ escape of $MnO_x$−$CeO_2$ mixed oxides as a low-temperature SCR catalyst. *Catal. Commun.* **2015**, *69*, 188−192.
(59) Zhang, Y.; Zhu, X.; Shen, K.; Xu, H.; Sun, K.; Zhou, C. Influence of ceria modification on the properties of $TiO_2$−$ZrO_2$ supported $V_2O_5$ catalysts for selective catalytic reduction of NO by $NH_3$. *J. Colloid Interface Sci.* **2012**, *376*, 233−238.
(60) Jiang, B.; Zhao, S.; Wang, Y.; Wenren, Y.; Zhu, Z.; Harding, J.; Zhang, X.; Tu, X.; Zhang, X. Plasma-enhanced low temperature $NH_3$-SCR of $NO_x$ over a Cu-Mn/SAPO-34 catalyst under oxygen-rich conditions. *Appl. Catal. B: Environ.* **2021**, *286*, No. 119886.
(61) Li, J.; Guo, J.; Shi, X.; Wen, X.; Chu, Y.; Yuan, S. Effect of aluminum on the catalytic performance and reaction mechanism of Mn/MCM-41 for $NH_3$-SCR reaction. *Appl. Surf. Sci.* **2020**, *534*, No. 147592.



https://doi.org/10.1021/acsomega.3c00718
*ACS Omega* 2023, 8, 13384−13395